nature physics

SUPPLEMENTARY INFORMATION

DOI: 10.1038/NPHYS3178

# Observation of magnetic field generation via the Weibel instability in interpenetrating plasma flows

## OMEGA Experimental Details

The experimental geometry consists of a pair of polyethylene ($CH_2$) plastic foils of diameter 2 mm and thickness 500 $\mu$m were oriented face-on, separated by 8 mm. Each was irradiated with 8 overlapped laser beams from the OMEGA laser, delivering $\approx$4 kJ of 351 nm laser energy in a 1 ns square pulse. Distributed phase plates were used to produce super-Gaussian laser spots with focal spot diameters of 250 $\mu$m on the target surface. The expanding plasma plumes interact at the midplane between the targets.

After a delay of 3 - 5 ns from the beginning of the drive pulse, the proton probe was created by compressing a thin-walled $SiO_2$ capsule with 18 beams, delivering $\approx$9 kJ total laser energy. The capsule was filled with a 1:1 mixture of deuterium (D) and $^3$helium ($^3$He) at a total pressure of 18 atm. At peak compression ($10^{23}$ cm$^{-3}$), protons are produced quasi-isotropically at 3.0 MeV through DD reactions, and at 14.7 MeV through fusion of D and $^3$He [1, 2]. The details of proton imaging have been treated at length in literature (see [3] and references therein), and proton probing has been used in numerous high-energy-density experiments on OMEGA and elsewhere to image electric and magnetic field structures (See [4] and references therein). The protons were detected using CR39 nuclear track detector positioned on the midplane of the $CH_2$ target foils, such that the protons traverse the central interaction region as shown in Fig. 1 of the main text.

## 3D OSIRIS Simulations

The PIC simulations presented here were done with the fully electromagnetic, fully relativistic, and massively parallel code OSIRIS [5, 6]. The code solves Maxwell's equations directly, resolving all the relevant physics at the electron and ion skin depth scales. The relativistic Lorentz force is used to calculate the motion of the plasma particles, and relativistic expressions are used to derive the charge and current densities from the positions and momenta of the particles.

DOI: 10.1038/NPHYS3178

Plasma electromagnetic and electrostatic instabilities arise in the simulations from first principles, as the simulations use a fully kinetic model for the plasma particles.

The simulation used to study the interaction between counter-streaming plasma flows has a box size of 1.3 cm (90 c/$\omega_{pi}$) in each direction and ran for a total of 6 ns ($\approx 1.7 \times 10^4 \omega_{pi}^{-1}$). Each plasma flow is composed by an electron and ion species (assumed to be fully ionized and modeled with $m_i/(Z \times m_e) = 128$). The numerical parameters were as follows: the 3D simulations used at least 2 cells per electron skin depth, 22 cells per ion skin depth, and 2 particles per cell per species, for a total of 70 billion particles. Due to the outstanding computational requirements, the 3D simulation ran in 131,072 cores in the supercomputer Mira (ANL). All simulations used cubic particle shapes, and current and field smoothing with compensation for improved numerical properties. Additional 2D simulations (not shown here) were done with higher resolution, greater number of particles per cell, and realistic ion to electron mass ratio ($m_i/(Z \times m_e) = 2048$), confirming overall result convergence consistent with the 3D results and showing that the ion Weibel instability can be reasonably scaled between systems with different mass ratios and (non-relativistic) flow velocities [7]. Additional detailed analysis of the simulations performed will be presented in a separate publication.

The simulated proton radiographs were obtained by launching a 14.7 MeV proton beam transversely to the flow propagation direction. The proton distribution was initialized in OSIRIS following the distribution of an isotropic point source located 1 cm away from the beginning of the simulation box, in order to be consistent with our experimental setup. The protons probe the self-consistent fields produced in the 3D simulation and exit on the opposite side of the simulation box, being then propagated ballistically to a square detector of 13 cm $\times$ 13 cm placed 30 cm away from the original point source, matching the experimental magnification of 30$\times$. The detector has 512 $\times$ 512 points, and $\sim$ 10 million probing protons are collected in each image.

## Interpretation of field structure from proton radiographs

The interpretation of proton images from complex systems must take into account the susceptibility of protons to deflections by both electric and magnetic fields. One can break the degeneracy between $E$ and $B$ fields is by comparing the relative deflection of higher and lower energy protons [3, 8, 9]. The distinct proton populations produced by the D$^3$He implosion lend themselves to this method. For the respective fields $E$ and $B$, the particle deflection $\sigma$ is given by:

$$\theta_B = \frac{q}{\sqrt{2 m_p E_p}} \int B_\perp dl \tag{1}$$

$$\theta_E = \frac{q}{2 E_p} \int E_\perp dl. \tag{2}$$

Thus, the ratio of deflection for 14.7 and 3 MeV protons expected from B-fields is $\theta_{DD}/\theta_{D^3He} \propto \sqrt{14.7/3} \approx 2.2$, while from E-fields one expects $\theta_{DD}/\theta_{D^3He} \propto$

$14.7/3 \approx 4.9$.

While the ratios above could in principle be directly measured, the complex, 3D structure of the system under investigation makes a quantitative comparison between low and high-energy proton images difficult. However, the similarity between the images from 3.0 and 14.7 MeV protons suggests deflection of the protons by magnetic fields. In particular, the same filaments can be co-registered between the two images, at decreased contrast in the image from 3.0 MeV protons. This is consistent with deflection from magnetic fields; were the deflection of the lower-energy protons 4.9× greater than the high-energy particles, the protons deflected by the small-scale filaments that are clear in the $D^3He$ image would be more diffuse in the DD image. Similarly, were the horizontal "plates" the result of electric fields, the difference in the position and contrast between the two proton energies would be larger, closer to 4.9×, which is not seen in the data.

The implementation of the toroidal Biermann-like fields into the 3D PIC simulations has been described in the main text; we comment here on the effect of these fields on the Weibel filaments that are the focus of this work. It is important to note that in the experiment, the Biermann battery and Weibel-generated fields are effectively independent of each other. The Biermann fields are the result of gradients in density and temperature ($\dot{B} \propto \nabla T_e \times \nabla n_e$), which arise naturally in the ablated plasma flows. However, these fields are strongest near the surface of the targets where the transverse gradients are largest, and are zero on-axis, where the Weibel instability mediated fields are strongest. In addition to this spatial separation, the Biermann battery and Weibel modes are also clearly separated in $k$-space, inhibiting efficient coupling between the two. The presence of the large-scale structure (the horizontal "plates") in the proton radiographs is related to this difference in scales–the large spatial extent of the Biermann fields generates a sizable proton deflection (related to $\int B \cdot dL$), despite their relatively low field strength.

## Analytic treatment of growing modes

To assess the susceptibility of the plasma in our experiment to Weibel growth, we have performed a linear stability analysis based on the collisionless Vlasov equation [10]. Using the same techniques as previous studies [11, 12], we arrived at the dispersion relation properly accounting for the chemical composition of the target. Such a description is necessary for multi-species plasmas, including the present system consisting of carbon and hydrogen. The results of this analysis show that the linear growth rate for a plasma with temperature of ∼1 keV, as measured in the system of interest, is sufficient for Wiebel filaments to reach a well-developed state during the first 1-2 ns of interaction between the plasma flows (3 - 4 ns after the initial laser drive). This agrees well with the growth observed in both experiment and simulation.

The linear dispersion relation for the filamentation instability driven by counter-streaming ion flows has been considered in a number of papers. The most relevant for our analysis are Refs.[11, 12]. In our experiment, we need to

DOI: 10.1038/NPHYS3178

consistently account for the presence of multiple ion species; the presence of the light ions leads to an enhancement in the stabilizing effect of a finite ion temperature. For the electromagnetic Weibel mode propagating perpendicularly with respect to the flow direction, the dispersion relation reads as:

$$k_x^2c^2+\frac{\omega_{pe}^2}{1+\frac{|k|}{\Gamma}\sqrt{\frac{2T_e}{\pi m_e}}}+\omega_{pi}^2\sum C_\alpha\left[G_1\left(\frac{\Gamma^2A_\alpha m_p}{2k^2T_\alpha}\right)-\frac{k_x^2v^2}{\Gamma^2}G_2\left(\frac{\Gamma^2A_\alpha m_p}{2k^2T_\alpha}\right)\right]=0, \tag{3}$$

Here $c$ is the speed of light and $k$ is the wave number perpendicular to the flow direction. The flow velocity is $v$, subscript "e" refers to the electron parameters, the subscript "$\alpha$" refers to the parameters of a certain ion species. We consider symmetric flows for which the unstable mode is the mode of an exponential growth. It is assumed that the electron thermal velocity exceeds the flow velocity, a condition that usually holds by a very large margin both in the laboratory and non-relativistic astrophysics. The growth rate is denoted by $\Gamma$, and $G_1$ and $G_2$ are dimensionless functions defined for $y>0$ as

$$G_1(y)=\frac{1}{\sqrt{\pi}}\int_{-\infty}^{+\infty}\frac{ye^{-x^2}}{x^2+y}dx; \tag{4}$$

$$G_2(y)=\frac{2y}{\sqrt{\pi}}\int_{-\infty}^{+\infty}\frac{x^2e^{-x^2}}{x^2+y}dx. \tag{5}$$

Additionally, one has

$$\omega_{pi}^2=\frac{4\pi e^2}{m_p}\sum_\alpha\frac{Z_\alpha^2}{A_\alpha}n_\alpha, \tag{6}$$

$$\omega_{pe}^2=\frac{4\pi e^2}{m_e}\sum_\alpha n_\alpha, \text{ and} \tag{7}$$

$$C_Z=\frac{n_\alpha Z_\alpha^2/A_\alpha}{\sum\limits_\alpha n_\alpha Z_\alpha^2/A_\alpha}. \tag{8}$$

Here $m_e$ and $m_p$ are the electron and proton mass, $Z_\alpha$, $A_\alpha$ and $n_\alpha$ are the charge, the atomic number and the particle density of the ion species $\alpha$.

By introducing dimensionless units for the wave number and growth rate,

$$\tilde{\Gamma}=\Gamma\frac{c}{v\omega_{pi}} \tag{9}$$

$$\tilde{k}=k_x\frac{c}{\omega_{pi}}. \tag{10}$$

one can recast the dispersion relation to the dimensionless form:

$$\tilde{k}^2+\frac{a_1}{1+\sqrt{\frac{a_2}{\pi}}\frac{|\tilde{k}|}{\tilde{\Gamma}}}+\sum C_Z\left[G_1\left(\frac{a_{3\alpha}\tilde{\Gamma}^2}{\tilde{k}^2}\right)-\frac{\tilde{k}^2}{\tilde{\Gamma}^2}G_2\left(\frac{a_{3\alpha}\tilde{\Gamma}^2}{\tilde{k}^2}\right)\right]=0, \tag{11}$$

where

$$a_1 = \frac{\omega_{pe}^2}{\omega_{pi}^2}, \tag{12}$$

$$a_2 = \frac{2T_e}{m_e v^2}, \quad \text{and} \tag{13}$$

$$a_{3\alpha} = \frac{2T_\alpha}{A_\alpha m_p v^2}. \tag{14}$$

This form allows one to more readily compare the results of simulations and experiments between systems, including astrophysical systems. The characteristic dispersion curves for the conditions of the OMEGA experiment are shown in Fig. 1.

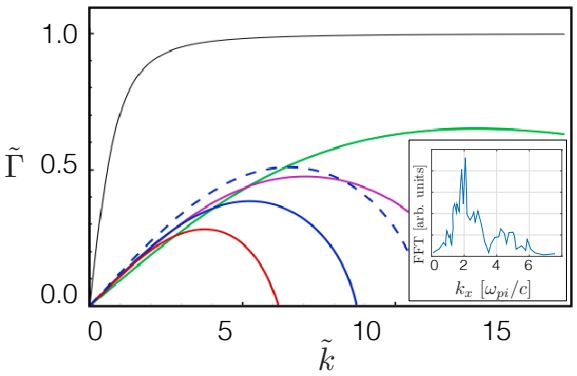


Figure 1: The linear Weibel growth rate $\tilde{\Gamma}$ vs the wave number $\tilde{k}$. The green, magenta, blue, and red curves correspond to $CH_2$ flows at electron and ion temperatures of 0.1 keV (green), 0.5 keV (magenta), 1 keV (blue) and 2 keV (red). The maximum growth rate for the electron density of $10^{19}$ cm$^{-3}$ in the $CH_2$ plasma is $0.5 \times 10^{10}$ $s^{-1}$ for blue curve. The dashed blue curve is for pure carbon at $T_e = T_i = 1$ keV, so that the difference between the solid and dashed blue curves is a manifestation of stabilization by the light ions. The black curve is a reference growth rate $\Gamma = kv\omega_{pi}/\sqrt{k^2c^2 + \omega_{pi}^2}$. Finally, the inset plot shows the magnetic field mode distribution from simulations. Here $k_x$ is transverse to the flow and measured after 2 ns of flow interaction, showing a range of unstable modes observed consistent with theoretical analysis.

DOI: 10.1038/NPHYS3178

## References


[1] M. J.-E. Manuel, A. B. Zylstra, H. G. Rinderknecht, D. T. Casey, M. J. Rosenberg, N. Sinenian, C. K. Li, J. A. Frenje, F. H. Séguin, and R. D. Petrasso. Source characterization and modeling development for monoenergetic-proton radiography experiments on omega. *Review of Scientific Instruments*, 83(6):063506, 2012.

[2] C. K. Li, F. H. Séguin, J. A. Frenje, *et al.* Monoenergetic proton backlighter for measuring e and b fields and for radiographing implosions and high-energy density plasmas (invited). *Review of Scientific Instruments*, 77(10):10E725, 2006.

[3] N. L. Kugland, D. D. Ryutov, C. Plechaty, J. S. Ross, and H.-S. Park. Invited article: Relation between electric and magnetic field structures and their proton-beam images. *Review of Scientific Instruments*, 83(10):101301, 2012.

[4] A. B. Zylstra, C. K. Li, H. G. Rinderknecht, F. H. Séguin, R. D. Petrasso, C. Stoeckl, D. D. Meyerhofer, P. Nilson, T. C. Sangster, S. Le Pape, A. Mackinnon, and P. Patel. Using high-intensity laser-generated energetic protons to radiograph directly driven implosions. *Review of Scientific Instruments*, 83(1):013511, 2012.

[5] R. Fonseca, L. Silva, F. Tsung, V. Decyk, W. Lu, C. Ren, W. Mori, S. Deng, S. Lee, T. Katsouleas, and J. Adam. Osiris: A three-dimensional, fully relativistic particle in cell code for modeling plasma based accelerators. In Peter Sloot, Alfons Hoekstra, C. Tan, and Jack Dongarra, editors, *Computational Science, ICCS 2002*, volume 2331 of *Lecture Notes in Computer Science*, pages 342–351. Springer Berlin / Heidelberg, 2002.

[6] R A Fonseca, S F Martins, L O Silva, J W Tonge, F S Tsung, and W B Mori. One-to-one direct modeling of experiments and astrophysical scenarios: pushing the envelope on kinetic plasma simulations. *Plasma Physics and Controlled Fusion*, 50(12):124034, 2008.

[7] D D Ryutov, N L Kugland, H S Park, C Plechaty, B A Remington, and J S Ross. Basic scalings for collisionless-shock experiments in a plasma without pre-imposed magnetic field. *Plasma Physics and Controlled Fusion*, 54(10):105021, 2012.

[8] C K Li, F H Séguin, J A Frenje, *et al.*. Diagnosing indirect-drive inertial-confinement-fusion implosions with charged particles. *Plasma Physics and Controlled Fusion*, 52(12):124027, 2010.

[9] C. K. Li, F. H. Séguin, J. A. Frenje, R. D. Petrasso, P. A. Amendt, R. P. J. Town, O. L. Landen, J. R. Rygg, R. Betti, J. P. Knauer, D. D. Meyerhofer, J. M. Soures, C. A. Back, J. D. Kilkenny, and A. Nikroo. Observations of

electromagnetic fields and plasma flow in hohlraums with proton radiography. *Phys. Rev. Lett.*, 102:205001, May 2009.

[10] Tsunehiko N. Kato and Hideaki Takabe. Electrostatic and electromagnetic instabilities associated with electrostatic shocks: Two-dimensional particle-in-cell simulation. *Phys. Plasmas*, 17:032114, 2010.

[11] Ronald C. Davidson, David A. Hammer, Irving Haber, and Carl E. Wagner. Nonlinear development of electromagnetic instabilities in anisotropic plasmas. *Physics of Fluids*, 15(2):317–333, 1972.

[12] R. L. Berger, J. R. Albritton, C. J. Randall, E. A. Williams, W. L. Kruer, A. B. Langdon, and C. J. Hanna. Stopping and thermalization of interpenetrating plasma streams. *Physics of Fluids B: Plasma Physics*, 3(1):3–12, 1991.